Journal of Vacuum Science and Technology A

RESEARCH ARTICLE | MAY 15 2024

Piezoelectric and elastic properties of $Al_{0.60}Sc_{0.40}N$ thin films deposited on patterned metal electrodes

Marco Liffredo ; Nan Xu ; Silvan Stettler ; Federico Peretti ; Luis Guillermo Villanueva

J. Vac. Sci. Technol. A 42, 043404 (2024)
https://doi.org/10.1116/6.0003497

16 May 2024 10:52:57

JVST A
Journal of Vacuum Science & Technology A
ARTICLE
pubs.aip.org/avs/jva

Piezoelectric and elastic properties of $Al_{0.60}Sc_{0.40}N$ thin films deposited on patterned metal electrodes

Cite as: J. Vac. Sci. Technol. A **42**, 043404 (2024); doi: 10.1116/6.0003497
Submitted: 30 January 2024 · Accepted: 25 April 2024 ·
Published Online: 15 May 2024

View Online Export Citation CrossMark

Marco Liffredo,[a)] Nan Xu, Silvan Stettler, Federico Peretti, and Luis Guillermo Villanueva

AFFILIATIONS

EPFL Laboratory of Advanced NEMS, MED 3 1426, Route Cantonale, Lausanne 1015, Switzerland

[a)] **Author to whom correspondence should be addressed:** marco.liffredo@epfl.ch

ABSTRACT

Sc-doped aluminum nitride (AlScN) allows for piezoelectric devices with large electromechanical coupling and the benefits increase with larger Sc doping in the film. However, with a larger Sc concentration, the process window narrows, and it is necessary to fine-tune the deposition parameters to achieve a good film. In this paper, we investigate depositions of highly doped AlScN (40% Sc) on unpatterned and patterned metal layers, to show how it is possible to maintain a good film quality on a metal electrode. We find how high-temperature deposition of the metal improves the AlScN film quality, how the gas mixture allows to reduce defects, and how film quality changes with thickness. We show that extreme care must be taken in the apparently trivial step of photoresist cleaning. Finally, we extract the mechanical, electrical, and piezoelectric properties of our optimized layer from a batch of fabricated resonators, obtaining a 5× improvement of piezoelectric coupling compared to undoped AlN and a 1.5× improvement from 32% doped AlScN.

16 May 2024 10:52:57

© 2024 Author(s). All article content, except where otherwise noted, is licensed under a Creative Commons Attribution (CC BY) license (https://creativecommons.org/licenses/by/4.0/). https://doi.org/10.1116/6.0003497

I. INTRODUCTION

Of all the members of the large family of piezoelectric materials, aluminum nitride (AlN) is one of the most widely employed because of its high acoustic velocity and quality factor, and established deposition and fabrication technology,[1] whose low deposition temperature makes it compatible with Front End of Line semiconductor processing. Leading applications of AlN lie in telecommunication filters,[2] oscillator components,[3] energy harvesting,[4] and piezoelectric micromachined ultrasound transducers (PMUTs).[5] While AlN has many points in favor, its drawback is the limited piezoelectric coupling that impacts the efficiency of electromechanical transduction. Rare-earth doping of AlN by substituting the Al atoms improves the coupling coefficient.

Substitution of Al atoms with Scandium atoms in the wurtzite structure of AlN (Sc-doped AlN or AlScN for short) causes a stretch of the lattice parameter and an increase in the dipole moment. Larger concentrations of Sc doping in AlScN result in larger crystal strain[6] and larger piezoelectric coefficient, both predicted by theory and demonstrated experimentally.[7,8] This monotonic trend is limited by the different phases of pure scandium nitride (ScN), which has its most stable phase as a not piezoelectric rock-salt cubic structure. The limitation of Sc doping arises when the formation enthalpy of the rock-salt phase is lower than the one of the wurtzite structure.[9] This allows for the formation of ternary compounds Al-Sc-N with the wurtzite structure of pure AlN. Experimentally, the maximum concentration of Sc in AlScN has been reported as 43%,[10] deposited at 400 °C. The challenge in deposition consists of the narrowing of the process window with the increase in Sc concentration in the film.

Deposition of AlN is mostly done using reactive sputtering[11,12] because such a process allows for post-CMOS compatibility of the piezoelectric production process.[2,13] Reactive sputtering of AlN and AlScN can be performed in RF or pulsed DC mode, the latter being the deposition method used for this paper. Reactive sputtering temperatures usually lie in the 300–500 °C range with some research done on AlN at temperatures up to 800 °C.[14,15] Including Sc in the deposition can be done via single-target sputtering of a cast Al-Sc alloy[16] or co-sputtering of Al and Sc targets using two separate plasma sources. In either case, the optimal deposition

© Author(s) 2024

temperature for AlScN has been reported to be around 400 °C[10,17] or lower, with higher (800 °C) temperature annealing showing a negative impact on the quality of the layers.[18] Other parameters affecting the film's quality are gas flow/pressure, gas partial pressure in the chamber, substrate bias, and underlying layer, among others.

In this paper, we investigate how different deposition parameters impact the overall quality of thin films of AlScN with 40% Sc concentration, we chose to study the properties of highly doped AlScN, being close to the maximum of 43% with a safety margin to avoid going above it and to keep the wurtzite structure. We show how a synergy of different deposition settings allows us to minimize abnormally oriented grains (AOGs) and XRD rocking curve full width half maximum (RC-FWHM). Then, we investigate how to deposit $Al_{0.6}Sc_{0.4}N$ on a patterned metal electrode aiming for the same film quality as a wafer fully covered with metal. Last, we fabricate a series of resonators with different electrode pitches to extract the acoustic and piezoelectric parameters and we compare our results to the literature.

II. EXPERIMENTS

A. $Al_{0.6}Sc_{0.4}N$ depositions

We deposit all the $Al_{0.6}Sc_{0.4}N$ and metal thin films described in this paper with a multichamber, single-target sputtering cluster Spider600 (Pfeiffer, Germany). Each process module of the cluster allows for gas lines of argon or nitrogen; sputtering is done in DC for metals and pulsed DC at 2 kHz for AlScN. The substrates can be heated up to 350 °C in a stable manner without straining the tool heaters and RF bias can be applied to increase the sputtered ions energy. RF bias is controlled by setting the DC power supplying the generator and can be used for in-chamber wafer cleaning with Ar etching. The distance between the target and wafer holder is 42.6 mm, the idle pressure without gas flowing in the process modules is 5×10^{-7} mbar, and the throttle valve setting results in a pressure of 5×10^{-3} mbar during deposition.

The sputtering targets are 6 mm in thickness and 200 mm in diameter, with a purity level of 99.95% for Pt, 99.9995% for Al, and 99.995% for Ti. $Al_{0.6}Sc_{0.4}N$ is reactively sputtered from an Al-Sc casted target with Sc = 40 at. % (52.6% mass ratio) and purity 99.99%. Before deposition, each target is cleaned by sputtering on a dummy wafer in a pure Ar atmosphere; for the $Al_{0.6}Sc_{0.4}N$ depositions, after the target cleaning, the chamber is conditioned by sputtering for 20 min in 50 SCCM of N_2 and the deposition is performed in poisoned target mode. For the depositions performed at high temperatures, the substrate holder is heated with a 90-min ramp before target cleaning.

Thin films are deposited on double-side polished high-resistive (HR) silicon ⟨100⟩ wafers (>10 kΩ cm), 100 mm in diameter, and 525 μm thick with a Ti-Pt layer to act as a bottom electrode and growth promotion layer. In previous experiments,[19] we observed a difference in the film quality between test wafers and HR wafers, so since the final devices require to be fabricated on HR substrates, this paper focuses the optimization only on the latter. We deposit a thin Pt layer on the top of the $Al_{0.6}Sc_{0.4}N$ film for better contrast when imaging with the SEM, since a conductive layer allows for better resolution of surface texture.

B. Film characterization

To characterize the film crystallinity, we use a Bruker D8 TXS X-ray diffractometer, with a rotating anode source and Eiger 500 2D detector, performing theta-2theta, Rocking Curves, and Reciprocal space mapping scans. To evaluate the number of AOGs, we use a Zeiss Merlin SEM at a magnification of 10 000×. AOG count is done using the Particle analysis function of FIJI.[20] Since we

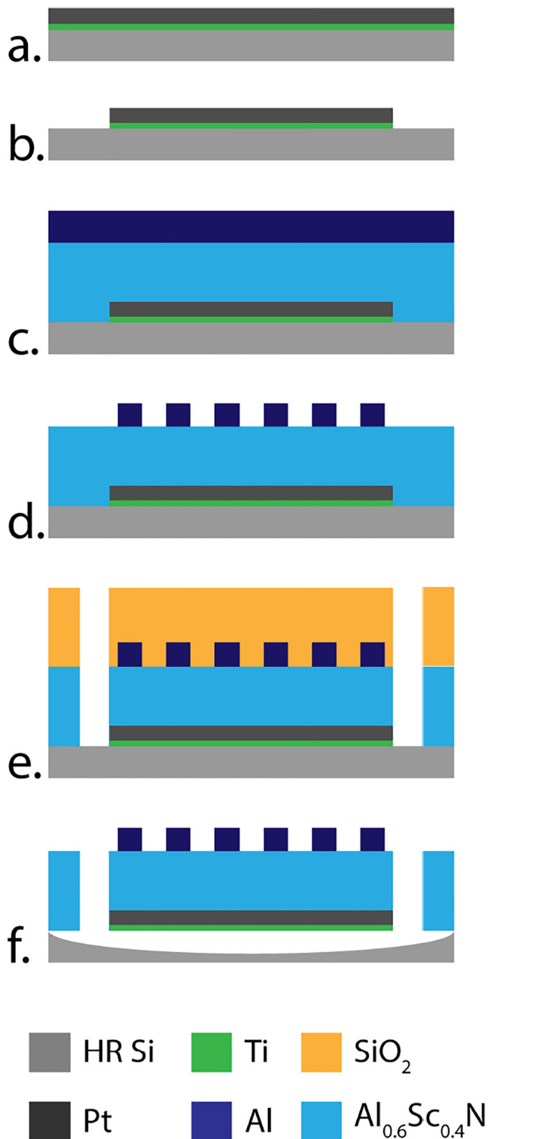

FIG. 1. Simplified process flow of the resonator fabrication: (a) deposition of the Ti adhesion layer and Pt bottom electrode, (b) patterning with IBE and resist strip, (c) deposition of AlScN layer and top electrode, (d) patterning of the top electrode and resist strip, (e) hard mask deposition and etching of AlScN, and (f) hard mask strip and XeF2 release.

16 May 2024 10:52:57

© Author(s) 2024

use the same magnification for every picture, the number of AOG reported in this paper is always referred to an area of 90 μm^2.

C. Device fabrication and characterization

To correlate the deposition conditions with the performance of $Al_{0.6}Sc_{0.4}N$ thin films, we fabricate lamb-wave resonators with a process flow adapted from Lozzi *et al.*,[21] with modifications to make it compatible with high-temperature depositions of the bottom electrode. We chose lamb-wave resonators[22] because their design allows us to measure both lateral vibrating and thickness vibrating modes. The resonance frequency of lateral vibration modes can be defined mostly via lithography, while for thickness vibrating modes the frequency is mostly defined by the layer thickness. This way one can obtain information on most elastic and piezoelectric coefficients of the film.

The first step in the fabrication of these resonators is the sputtering of the bottom electrode on the Si substrate, as seen in Fig. 1(a). The platinum bottom electrode nucleates with a ⟨111⟩ orientation, which promotes the growth of (0002) AlScN.[23] To promote the adhesion of the Pt layer on Si, we deposit 10 nm of Ti, while the Pt thickness is 25 nm.

The bottom electrode is then patterned using dry etching after a lithography step using AZ ECI 3007 (MicroChemicals GmbH, Germany) as a photoresist, and a SUSS MA6 mask aligner equipped with a broadband Hg lamp source for exposure. Pt is etched using a Nexus IBE350 Ion Beam Etching tool (IBE, Veeco, USA), with an Ar ion beam current of 800 mA/cm^2 and an acceleration voltage of 500 V [Fig. 1(b)]. Deposition of the piezoelectric $Al_{0.6}Sc_{0.4}N$ layer and the top Pt electrode is performed without breaking the vacuum directly on Pt. The target thicknesses are 400 nm of $Al_{0.6}Sc_{0.4}N$ and 50 nm of Al [Fig. 1(c)]. After another lithography step, the top electrodes are patterned [Fig. 1(d)] with Cl_2/BCl_3 inductively coupled plasma reactive ion etching (RIE, SPTS Ltd, UK). A SiO_2 hard mask is then deposited with RF sputtering, to be patterned, after lithography, using a C_4F_8 ICP RIE, and subsequently used as a mask for the $Al_{0.6}Sc_{0.4}N$ patterning in IBE [Fig. 1(e)]. Resonators are then released in XeF2 [Fig. 1(f)].

Fabricated resonators are then electrically characterized using an MPI 150 probe station equipped with dual GSG probes, connected to a ZNB20 Vector Network Analyzer (Rohde & Schwarz, Germany). We probe the devices from 100 MHz to 7.5 GHz with a power of −10 dBm. The measurements are then fitted to a modified Butterworth–Van Dyke[24] (mBVD) model to extract the parasitic and motional parameters.

III. RESULTS AND DISCUSSION

A. Full bottom deposition

This batch of experiments includes around 50 wafers, and, in every case, the bottom metal covers fully the wafer surface without patterning.

1. Adhesion layer temperature, bias power, and gas flow impact

The first tests focus on the evaluation of the impact on the deposition quality of temperature of the bottom metal electrode deposition, and substrate biasing and gas flow ratio during the AlScN deposition. The starting point of this work comes from the

16 May 2024 10:52:57

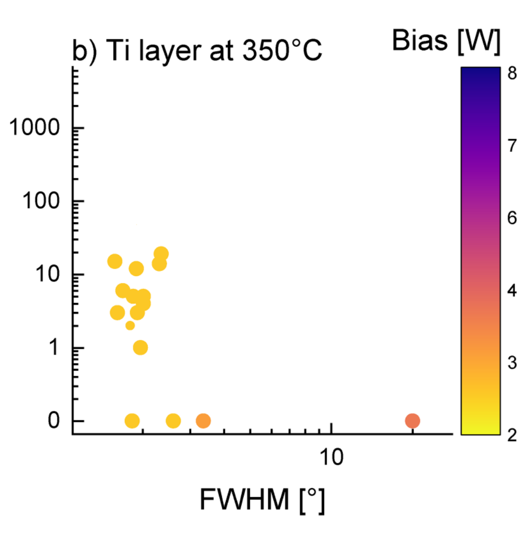

FIG. 2. Parametric plot of average AOG count in the inner 80 mm diameter of the wafer vs Rocking curve FWHM. (a) shows wafers where the Ti adhesion layer was deposited at room temperature (RT), while (b) shows wafers where Ti was deposited at 350 °C. Each marker represents a wafer, the size of the marker indicates the Ar percentage of gas flow, and the color represents the bias power applied to the wafer. The figure includes layers of thickness ranging from 100 to 1000 nm. A good quality film, with low AOG count and FWHM, can be obtained with a high temperature of Ti, low substrate RF bias power, and by including Ar in the sputtering mixture.

© Author(s) 2024

findings reported in the doctoral thesis of Howell[19] and Sandu *et al.*[25]

To investigate the temperature effect, we deposit the Ti adhesion layer at RT and 350 °C. We change the biasing power from 2 to 8 W and the Ar percentage in the sputtering mix from 0% to 60%. We do not increase further the Ar concentration to keep working in poison mode.

Figure 2 gives an overall snapshot of the impact of deposition conditions on film quality. In both groups of samples with Ti at RT and 350 °C, the rocking curve FWHM decreases with lower substrate bias applied. To make this trend clearer, we include Fig. 3 for both high-temperature Ti and RT Ti. This conclusion aligns with the findings of Sandu *et al.*[25] where the metrics for film quality is the improvement of Theta-2theta peak with a lower bias. From both Figs. 2 and 3, we observe that Temp of Ti and gas flow ratio do not have an enormous influence on the FWHM; however, they both significantly reduce the AOG count.

Overall, the best results are obtained with a 10–20 SCCM Ar flow together with a 30 SCCM N_2 flow, with Ti deposited at 350 °C, and 2 W of bias power, as visible in Fig. 3 bottom. The improvement of the $Al_{0.6}Sc_{0.4}N$ film quality with high-temperature Ti deposition agrees with the findings of Zhao *et al.*[26] We obtain an acceptable deposition quality by depositing the AlScN directly on Pt, without the need for an intermediate AlN seed layer.[27] The deposition rate for the different gas ratios does not seem to change significantly, being measured as 48 nm/min.

2. Effect of $Al_{0.6}Sc_{0.4}N$ thickness

We then take the optimal conditions found in the previous paragraph, to investigate the growth at different thicknesses. We deposit a series of wafers with the same process varying the $Al_{0.6}Sc_{0.4}N$ deposition time. As seen in Fig. 4, the FWHM stabilizes at around 1.6 °C for films thicker than 200 nm showing a plateau of film quality for thickness above that one. The number of AOG increases with the thickness, which is a sign of defects appearing during the deposition as reported elsewhere.[14] This result motivates the choice of 400 nm as the film thickness to fabricate the devices, which serve to extract the material properties of our layer. With

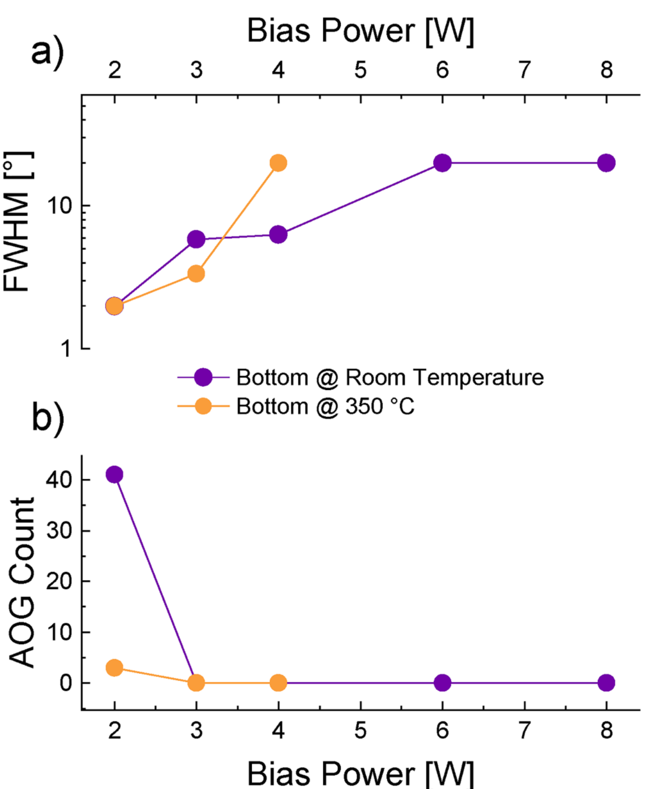

FIG. 3. Comparison between room temperature and 350 °C Ti. While FWHM (a) decreases in both cases with a lower bias power, the number of abnormal grains (b) at low bias is much higher when the Ti layer is at room temperature. All films have a thickness ranging from 400 to 500 nm, deposited with a gas flow of 30 SCCM N_2 and 20 SCCM Ar.

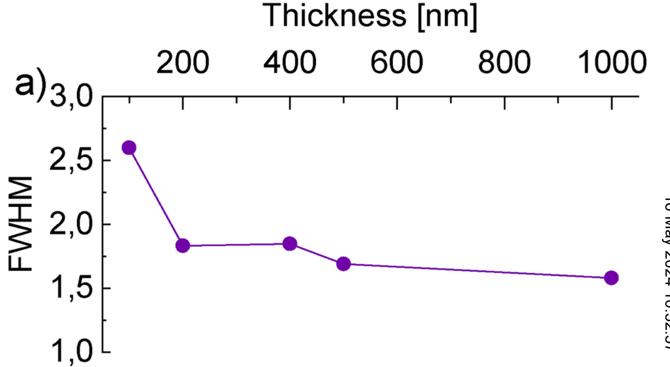

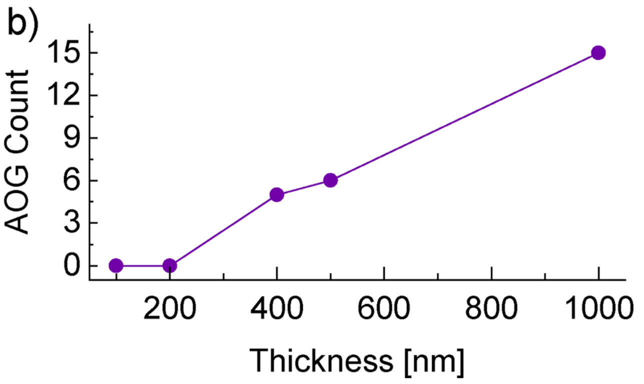

FIG. 4. Evolution of AOG density and FWHM with film thickness for the same depositing conditions (30 SCCM N_2 and 20 SCCM Ar, bottom layer at 350 °C and 2 W of bias power). The stabilization of FWHM (a) shows good nucleation from 200 nm of thickness while the increase of AOGs (b) with the thickness shows the impact of defects.

16 May 2024 10:52:57

© Author(s) 2024

FIG. 5. Comparison of SEM images of the wafer surface on a patterned Pt electrode. (a) shows the abundance of AOG on a wafer where the photoresist was stripped with only O_2 plasma dry ashing; (b) half shows the low number of AOG on a wafer where the photoresist was stripped with O_2 plasma—Remover 1165—O_2 plasma.

16 May 2024 10:52:57

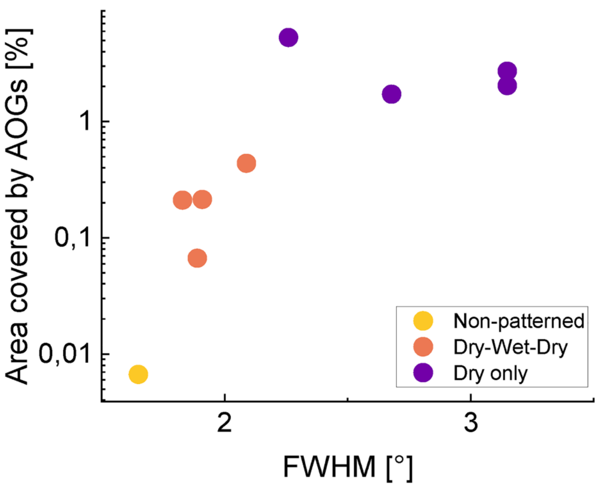

FIG. 6. Impact of cleaning procedure on deposition results: at the bottom left, the best film was obtained without patterning the Pt electrode ("Gold Standard"). Ideally, the devices with patterned bottom electrodes should have the same film quality. Cleaning of the photoresist by only using O_2 plasma results in a worse film quality than cleaning using the O_2 plasma—Remover 1165—O_2 plasma procedure, both regarding FWHM and the number of AOGs.

said thickness, the quality of the layer is optimal and many lamb-wave modes can be excited.[28]

3. Investigation of bottom Pt thickness and deposition temperature

An additional variation in this batch of experiments is the thickness and deposition temperature of the bottom Pt. The former is changed between 25 and 50 nm and no significant change in verticality, crystallinity, or AOG count can be observed. When comparing the latter, no significant change is observed between RT, 200 °C, or 350 °C for the FWHM. However, a slight reduction in the AOG count happens when the temperature of Pt deposition increases.

Since reducing the thickness of the bottom layer allows to limit the acoustic losses associated with the high density of platinum, from now on all wafers in the paper are fabricated with 25 nm of Pt deposited at the same temperature of 350 °C as Ti.

B. Bottom electrode patterning

Most studies for AlScN thin film deposition optimization are done with a bottom metal electrode covering the full surface of the wafer. This allows for good growth of AlScN and great

© Author(s) 2024

reproducibility since the vacuum is typically not broken during the deposition.

However, having bottom metal everywhere leads to an increased parasitic capacitance in the final device, thus reducing the electromechanical coupling. To optimize resonator performance, it is necessary to pattern the bottom metal layer to have metal only under the active area of the resonator. In previous iterations of our fabrication, the bottom metal layer was deposited at room temperature and the pattern was done via lift-off,[21,29] which allows for a clean bottom metal surface to facilitate the growth of the AlScN layer. As seen in Sec. A 1, film quality is better when the bottom Ti-Pt electrode is deposited at a high temperature. This bars us from using lift-off since the deposition temperature would melt the photoresists. Therefore, we move from lift-off to ion beam etching of the bottom metal layer. According to Ref. 30, the surface of a photoresist exposed to an ion beam will be chemically modified and become less reactive to the stripping technique, creating a "crust" of burnt resist. This crust of burnt resist increases the difficulty of obtaining a clean bottom metal surface, which must be as free of residues as possible.

In all tests, we etch the bottom metal with ion beam etching with a beam angle of 10°. To avoid fences due to the sputtering of Pt on the sidewalls of the photoresist, after exposure and development, the resist is baked at 125 °C for 2 min. This reflow slopes the sidewalls and no fences arise from the etching. After stripping, we deposit $Al_{0.6}Sc_{0.4}N$ and we analyze the number of AOG, with a particular interest in the region close to the interface between the Pt region and the Si region where the Pt is etched.

Standard recipes used for photoresist stripping in our cleanroom rely on O_2 plasma ashing or wet solvent removal. Since this step is critical, we experimented with two approaches. First, a fully dry approach—with 15 min of oxygen plasma (O_2 flow 400 SCCM, plasma power 600 W). The result is visible in Fig. 5(a): many abnormal grains both on Si and on Pt can be observed, indicating that residues of the burnt photoresist remain on the bottom Pt surface before AlScN deposition and, thus, foster the creation of defects in the film.

Second, a more refined approach involving three steps, a quick 1 min oxygen plasma treatment to open the crust of burnt photoresist, followed by wet stripping of the polymer with two 5 min baths in N-methyl-2-pyrrolidone solvent (Remover 1165, Dow Chemical, USA) heated at 70 °C. After wet stripping and rinsing, a second oxygen plasma step at 200 W with 200 SCCM O_2 flow is run for 3 min. The result of this three-step process is to lift-off the burnt resist layer by stripping the underlying undamaged portion of it. Results, visible in Fig. 5(b), show a decrease in abnormal grains compared to pure O_2 stripping but still a larger number than non-patterned Pt.

To quantify the impact of the cleaning technique on film quality, we plot in Fig. 6 the percentage of a scan surface covered with AOG. Since they do not generate a piezoelectric response, the percentage of the resonator area covered by AOGs must be minimized. For comparison, we include in this plot the result of one of the best wafers with full-bottom deposition. Wafers that have been cleaned with the three-step process have a lower area covered with AOGs and a better FWHM than the ones cleaned only with O_2 plasma ashing, getting closer in quality to our "gold standard" wafer.

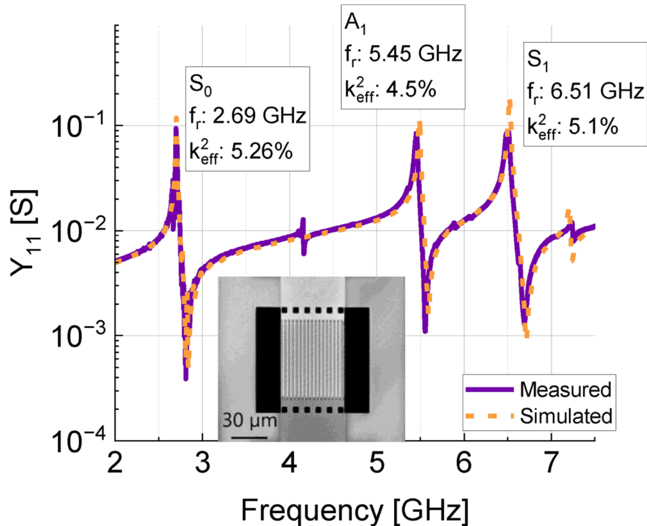

FIG. 7. Comparison between measured and simulated curves, used to extract the piezoelectric, stiffness, and permittivity matrix coefficients. Highlighted the resonance frequency and calculated effective k^2_{eff} of three of the modes used to extract the stiffness and piezoelectric matrices. The effective piezoelectric coupling coefficient is calculated from the BVD model static capacitance C_0 and motional capacitance C_m using the IEEE standard definition $C_m/(C_m + C_0)$ (Refs. 31 and 32). In the snippet in the figure, an SEM image of a suspended resonator is given.

16 May 2024 10:52:57

C. Resonator characterization and parameters extraction

Released resonators are characterized using GSG probes and a VNA. A typical response from 2 to 7.5 GHz is shown in Fig. 7. The responses show different peaks that can be identified with different resonant modes in the suspended devices. The frequency and coupling of each of the observed modes depend on the pitch and thus allow us to extract the material properties of our optimal layer using FEM simulations.

A 2D and a 3D FEM model is built using COMSOL MULTIPHYSICS to simulate the electrical, mechanical, and electromechanical behavior of our resonators. Lateral dimensions are

TABLE I. Extracted elastic and piezoelectric coefficients.

Property		Unit	$Al_{0.60}Sc_{0.40}N$
Density	ρ	g/cm^3	3.35
Elastic matrix	c_{11}	GPa	294 ± 1
	c_{13}	GPa	125 ± 5
	c_{33}	GPa	195 ± 5
	c_{44}	GPa	100 ± 2.5
Piezoelectric matrix	e_{15}	C/m^2	−0.20 ± 0.1
	e_{31}	C/m^2	−0.85 ± 0.1
	e_{33}	C/m^2	3.10 ± 0.1
Relative permittivity	$\varepsilon_{33}/\varepsilon_0$	—	28 ± 2
	$\varepsilon_{11}/\varepsilon_0$	—	19 ± 2

© Author(s) 2024

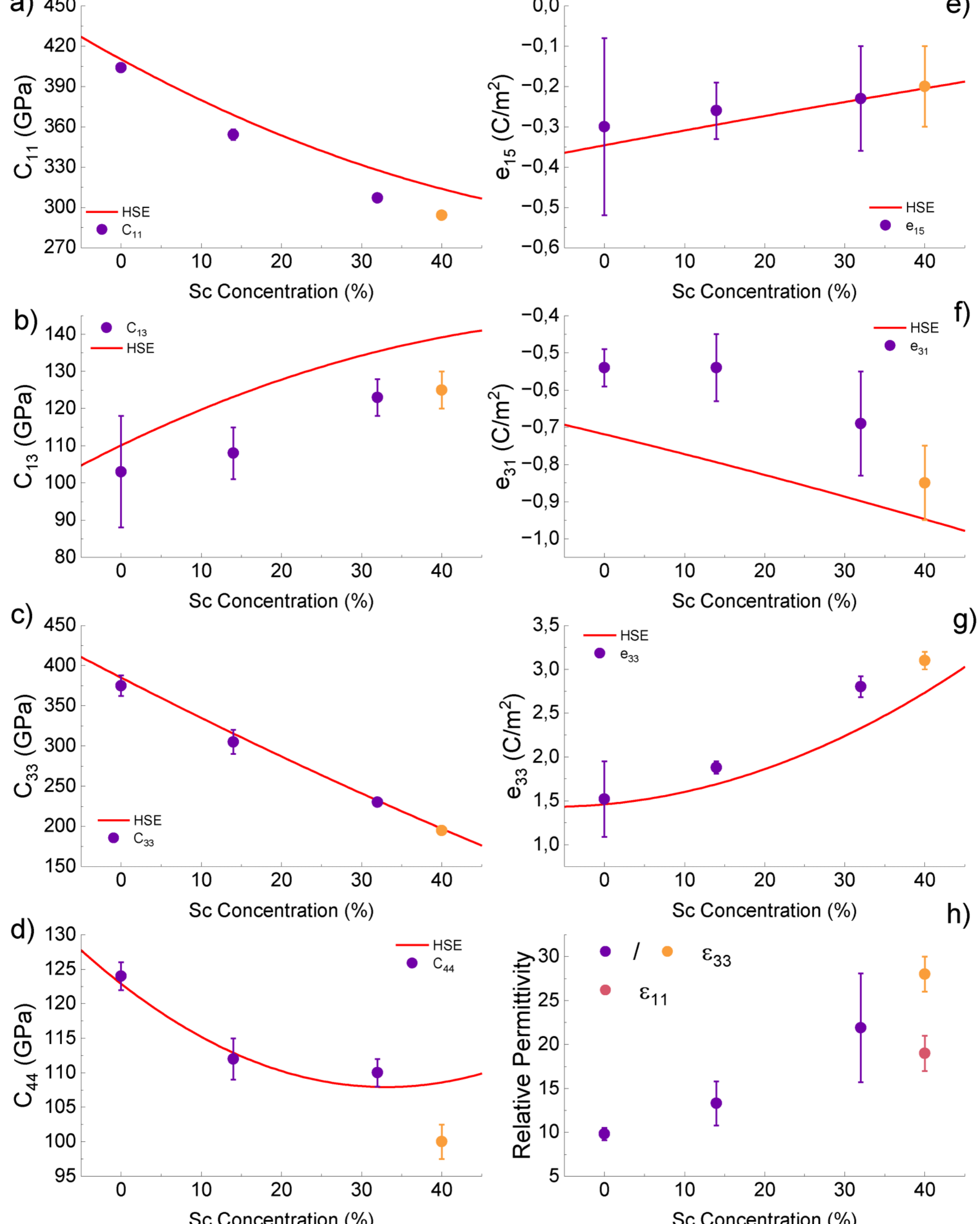

FIG. 8. Comparison with Kurz *et al.* (Ref. 34) in purple, values from 0–30% Sc concentration, our findings in yellow for 40% Sc concentration and trendlines extracted from Caro *et al.* (Ref. 33) (HSE-corrected) in a continuous line. Our best fitting resulted in an anisotropic value for relative permittivity [28 for ε_{33}, 19 for ε_{11} in (h)]. Stiffness matrix elements are plotted in (a)–(d), while piezoelectric matrix elements in (e)–(g).

16 May 2024 10:52:57

obtained via SEM analysis of each one of the measured devices (around 100). The thickness of the different layers is measured using ellipsometry and/or mechanical profilometry. The resulting measured thickness of the $Al_{0.6}Sc_{0.4}N$ layer was 397 nm while the measured thickness of the bottom electrode was 31 nm for bottom Pt and 14 nm for Ti, while the top metal thickness was 60 nm. Knowing the dimensions, only material properties determine the simulation results.

© Author(s) 2024

The metals are simulated using the bulk values for density and stiffness, while as a starting point for the material properties of $Al_{0.6}Sc_{0.4}N$, we take the stiffness and piezoelectric matrices from the density functional theory calculations of Caro *et al.*[33] For the relative permittivity and the density, the starting point comes, respectively, from interpolation and an extrapolation of the experimental results by Kurz *et al.*[34] Density is fixed and not changed in our simulations, whereas relative permittivity is allowed to change and even to be anisotropic in the out-of-plane direction.

More than 10^4 simulations are performed using different combinations of the material properties, allowing them to change around ±10% of the starting values. For the special case of in-plane dielectric permittivity, the results show a much better fit when allowing for it to be much smaller than the out-of-plane one. Each simulation allows us to compare between three and five resonant modes (both resonance and antiresonance) and the static capacitance. We use three dimensionless metrics to extract first the elastic properties $\left(M_1 = \sum_{i=1}^{N_{modes}} f_{r,i}^{\text{sim}} - f_{r,i}^{\text{exp}}/f_{r,i}^{\text{exp}}\right)$, then the dielectric properties $\left(M_2 = \sum_{i=1}^{N_{devices}} C_{0,i}^{\text{sim}} - C_{0,i}^{\text{exp}}/C_{0,i}^{\text{exp}}\right)$, and finally the piezoelectric properties $\left(M_3 = \sum_{i=1}^{N_{modes}} k_{eff,i}^{\text{sim}} - k_{eff,i}^{\text{exp}}/k_{eff,i}^{\text{exp}}\right)$. These metrics, we establish which material properties better fit the experimental data, taking into account the ensemble of devices and modes. We are also able to provide some confidence intervals for the estimated values, which are included in Table I.

To put these values in perspective, we plot them in Fig. 8 together with results from Kurz *et al.*[34] and some DFT predictions by Caro *et al.*[33] One can see how the data from our layer follows the same trend marked by previous works. Once again, it is interesting to highlight that the relative permittivity appears to be clearly anisotropic.

With these values, one can also estimate the d-piezoelectric matrix elements to be $d_{31} = 10 \pm 1(\text{pC}/N)$, $d_{33} = 29 \pm 3(\text{pC}/N)$, and $d_{15} = 2 \pm 0.2(\text{pC}/N)$. Further, we can also estimate the material electromechanical coupling for the vertically vibrating mode (Film Bulk Acoustic Resonator, FBAR) and the laterally vibrating mode (S0),

$$K_{S0}^2 = \frac{d_{31}^2}{\epsilon_{33}\epsilon_0 S_{11}} \sim 8\%,$$

TABLE II. Deposition parameters for resonator fabrication.

Process parameter	Value
Ti temperature	350 °C
Ti thickness	15 nm
Pt temperature	350 °C
Pt thickness	25 nm
AlScN temperature	300 °C
AlScN sputtering power	1500 W
AlScN substrate bias	2 W
AlScN N_2 flow	30 SCCM
AlScN Ar flow	10 SCCM
AlScN thickness	400 nm
Chamber pressure	4×10^{-3} mbar

$$K_{FBAR}^2 = \frac{e_{33}^2}{\epsilon_{33}\epsilon_0 C_{33}} \sim 20\%.$$

Calculation of the same values from Kurz results yields a K_{S0}^2 of 5% and a K_{FBAR}^2 of 18% showing the increase of coupling from 32% to 40% Sc concentration.

IV. SUMMARY AND CONCLUSIONS

In this paper, we show the impact of multiple deposition conditions on the quality of $Al_{0.6}Sc_{0.4}N$ films. We show how the deposition of Ti and Pt at high T and the inclusion of Ar in the sputtering atmosphere reduces the number of AOGs and results in a better verticality of the piezoelectric film growth. We analyze the impact of substrate biasing during deposition, showing that for high Sc doping levels better results are obtained with a very low bias. Our optimal deposition parameters are reported in Table II.

With the optimal recipe for deposition, the paper explores bottom metal patterning and shows how to mitigate the defects introduced by ion beam etching of the metal. The capability of having a high-quality film on a patterned bottom allows for a more flexible process that does not require a full conductive metal electrode, with lower parasitic capacitance and thus higher coupling.

Finally, using some fabricated resonators and their electromechanical response, material parameters are presented for our optimal layer. These properties are extracted after comparison to thorough manyfold FEM simulations. The properties match the trends marked by previous works in the literature.

To our knowledge, this is the first reported in-depth experimental analysis of the material properties of $Al_{0.6}Sc_{0.4}N$. This opens the possibility of more in-depth studies of resonator architecture and acoustic behavior. We believe this will allow for easier implementation of devices benefitting from high Sc concentration, like PMUTs,[35] field-effect transistors,[36] or devices for energy harvesting.[37] Future development will focus on the utilization of this layer in electromechanical filters for current and future communication bands.

16 May 2024 10:52:57

ACKNOWLEDGMENTS

The authors wish to thank Kaitlin Marie Howell for laying the groundwork for $Al_{0.6}Sc_{0.4}N$ depositions in the laboratory and the staff of the EPFL Center of MicroNanotechnology (a mention to Guy François Clerc, Remy Juttin, and Blaise Cuénod) for the continuous support, maintenance, and troubleshooting of the sputtering tools. This work was supported by the Swiss National Science Foundation with Grant Nos. 200020-184935, CRII5-189967, and 206021-205378.

AUTHOR DECLARATIONS

Conflict of Interest

The authors have no conflicts to disclose.

Author Contributions

Marco Liffredo: Conceptualization (equal); Investigation (lead); Validation (equal); Writing – original draft (lead). **Nan Xu:**

© Author(s) 2024

Data curation (supporting); Investigation (equal); Validation (supporting). **Silvan Stettler:** Data curation (equal); Methodology (equal); Software (lead). **Federico Peretti:** Investigation (equal); Software (supporting). **Luis Guillermo Villanueva:** Conceptualization (equal); Funding acquisition (lead); Project administration (equal); Resources (lead); Writing – original draft (supporting).

DATA AVAILABILITY

The data that support the findings of this study are available from the corresponding author upon reasonable request.

REFERENCES

[1]M.-A. Dubois and P. Muralt, Appl. Phys. Lett. **74**, 3032 (1999).
[2]R. C. Ruby, P. Bradley, Y. Oshmyansky, A. Chien, and J. D. Larson, in *2001 IEEE Ultrasonics Symposium Proceedings: An International Symposium (Cat No. 01CH37263)*, Atlanta, GA, 7–10 October 2001 (IEEE, New York, 2001), p. 813.
[3]A. Lozzi, M. Liffredo, E. T.-T. Yen, J. Segovia-Fernandez, and L. G. Villanueva, J. Microelectromech. Syst. **29**, 306 (2020).
[4]T.-T. Yen, T. Hirasawa, P. K. Wright, A. P. Pisano, and L. Lin, J. Micromech. Microeng. **21**, 085037 (2011).
[5]A. Guedes, S. Shelton, R. Przybyla, I. Izyumin, B. Boser, and D. A. Horsley, in *2011 International Solid-State Sensors, Actuators and Microsystems Conference*, Beijing, China, 5–9 June 2011 (IEEE, New York, 2011), p. 2062.
[6]N. Takeuchi, Phys. Rev. B **65**, 045204 (2002).
[7]G. Esteves, T. R. Young, Z. Tang, S. Yen, T. M. Bauer, M. D. Henry, and R. H. Olsson, Appl. Phys. Lett. **118**, 171902 (2021).
[8]R. H. Olsson, Z. Tang, and M. D'Agati, in *2020 IEEE Custom Integrated Circuits Conference (CICC)*, Boston, MA, 22–25 March 2020 (IEEE, New York, 2020), p. 1.
[9]K. Hirata, K. Shobu, H. Yamada, M. Uehara, S. A. Anggraini, and M. Akiyama, J. Eur. Ceram. Soc. **40**, 5410 (2020).
[10]M. Akiyama, K. Kano, and A. Teshigahara, Appl. Phys. Lett. **95**, 162107 (2009).
[11]M.-A. Dubois and P. Muralt, J. Appl. Phys. **89**, 6389 (2001).
[12]M. Akiyama, T. Kamohara, K. Kano, A. Teshigahara, Y. Takeuchi, and N. Kawahara, Adv. Mater. **21**, 593 (2009).
[13]M.-A. Dubois, C. Billard, C. Muller, G. Parat, and P. Vincent, in *ISSCC 2005 IEEE International Solid-State Circuits Conference, Digest of Technical Papers*, San Francisco, CA, 10 February 2005 (IEEE, New York, 2005), p. 392.
[14]C. S. Sandu, F. Parsapour, S. Mertin, V. Pashchenko, R. Matloub, T. LaGrange, B. Heinz, and P. Muralt, Phys. Status Solidi A **216**, 1800569 (2019).
[15]A. Zukauskaite *et al.*, J. Appl. Phys. **111**, 093527 (2012).
[16]M. Akiyama, T. Tabaru, K. Nishikubo, A. Teshigahara, and K. Kano, J. Ceram. Soc. Jpn. **118**, 1166 (2010).
[17]O. Zywitzki, T. Modes, S. Barth, H. Bartzsch, and P. Frach, Surf. Coat. Technol. **309**, 417 (2017).
[18]N. Wolff, M. R. Islam, L. Kirste, S. Fichtner, F. Lofink, A. Žukauskaitė, and L. Kienle, Micromachines **13**, 1282 (2022).
[19]K. M. Howell, *Dielectric Actuation Techniques at the Nanoscale: Piezoelectricity and Flexoelectricity* (EPFL, Lausanne, Switzerland, 2019).
[20]J. Schindelin *et al.*, Nat. Methods **9**, 676 (2012).
[21]A. Lozzi, E. Ting-Ta Yen, P. Muralt, and L. G. Villanueva, IEEE Trans. Ultrason. Ferroelectr. Freq. Control **66**, 146 (2019).
[22]H. Bhugra and G. Piazza, *Piezoelectric MEMS Resonators* (Springer International, New York, 2017).
[23]S. Fichtner *et al.*, J. Appl. Phys. **122**, 035301 (2017).
[24]J. D. Larson, P. D. Bradley, S. Wartenberg, and R. C. Ruby, in *2000 IEEE Ultrasonics Symposium Proceedings: An International Symposium* (Cat No. 00CH37121), San Juan, PR, 22–25 October 2000 (IEEE, New York, 2000), p. 863.
[25]C. S. Sandu, F. Parsapour, D. Xiao, R. Nigon, L. M. Riemer, T. LaGrange, and P. Muralt, Thin Solid Films **697**, 137819 (2020).
[26]X. Zhao, O. Kaya, M. Pirro, M. Assylbekova, L. Colombo, P. Simeoni, and C. Cassella, J. Microelectromech. Syst. **31**, 561 (2022).
[27]F. Parsapour, V. Pashchenko, S. Mertin, C. Sandu, N. Kurz, P. Nicolay, and P. Muralt, in *2017 IEEE International Ultrasonics Symposium (IUS)*, Washington, DC, 6–9 September 2017 (IEEE, New York, 2017), p. 1.
[28]G. Giribaldi, L. Colombo, and M. Rinaldi, IEEE Trans. Ultrason. Ferroelectr. Freq. Control **70**, 1 (2023).
[29]A. Lozzi, A. De Pastina, L. G. Villanueva, and E. T.-T. Yen, in *2017 IEEE International Ultrasonics Symposium (IUS)*, Washington, DC, 6–9 September 2017 (IEEE, New York, 2017), p. 1.
[30]K. Hirose, H. Shimada, S. Shimomura, M. Onodera, and T. Ohmi, J. Electrochem. Soc. **141**, 192 (1994).
[31]R. Lu, M.-H. Li, Y. Yang, T. Manzaneque, and S. Gong, J. Microelectromech. Syst. **28**, 209 (2019).
[32]IEEE Standard 176–1987: *IEEE Standard on Piezoelectricity* (IEEE, 1988).
[33]M. A. Caro, S. Zhang, T. Riekkinen, M. Ylilammi, M. A. Moram, O. Lopez-Acevedo, J. Molarius, and T. Laurila, J. Phys.: Condens. Matter **27**, 245901 (2015).
[34]N. Kurz, A. Ding, D. F. Urban, Y. Lu, L. Kirste, N. M. Feil, A. Žukauskaitė, and O. Ambacher, J. Appl. Phys. **126**, 075106 (2019).
[35]Q. Wang, Y. Lu, S. Mishin, Y. Oshmyansky, and D. A. Horsley, J. Microelectromech. Syst. **26**, 1132 (2017).
[36]X. Liu *et al.*, Nano Lett. **21**, 3753 (2021).
[37]P. Frach, S. Barth, H. Bartzsch, and D. Gloess, Proc. SPIE **10194**, 101942Z (2017).

16 May 2024 10:52:57

© Author(s) 2024